Multi-Stranded and Multi-Thermal Solar Coronal Loops: Evidence from Hinode X-Ray Telescope and EUV Imaging Spectrometer Data

J.T. Schmelz[1,2], S.H. Saar[2], K. Nasraoui[1], V.L. Kashyap[2], M.A. Weber[2], E.E. DeLuca[2], L. Golub[2]

ABSTRACT

Data from the X-Ray Telescope (XRT) and the EUV Imaging Spectrometer (EIS) on the Japanese/USA/UK *Hinode* spacecraft were used to investigate the spatial and thermal properties of an isolated quiescent coronal loop. We constructed Differential Emission Measure (DEM) curves using Monte Carlo based, iterative forward fitting algorithms. We studied the loop as a whole, in segments, in transverse cuts, and point-by-point, always with some form of background subtraction, and find that the loop DEM is neither isothermal nor extremely broad, with approximately 96% of the EM between $6.2 \leq \log T \leq 6.7$, and an EM weighted temperature of $\log T = 6.48 \pm 0.16$. We find evidence for a gradual change in temperature along the loop, with log T increasing only by $\approx$0.1 from the footpoints to the peak. The combine XRT-EIS date set does a good job of constraining the temperature distribution for coronal loop plasma. Our studies show that the strong constraints at high and low temperatures provided by the combined data set are crucial for obtaining reasonable solutions. These results confirm that the observations of at least some loops are not consistent with isothermal plasma, and therefore, cannot be modeled with a single flux tube and must be multi-stranded.

Subject headings: Sun: corona, Sun: X-ray radiation, Sun: fundamental parameters

1. Introduction

Observations since Skylab have shown that different types of loops exist in the solar corona. Some are more dynamic and seen mainly in transition region lines. Others occur

[1]Physics Department, University of Memphis, Memphis, TN 38152, jschmelz@memphis.edu

[2]Harvard-Smithsonian Center for Astrophysics, 60 Garden St., Cambridge, MA 02138

after a flare and are multi-thermal. Still others are more quiescent and longer lived; some of these appear to be isothermal. Most of the recent analysis on loop temperatures from coronal imagers such as the Yohkoh Soft X-ray Telescope (SXT; Tsuneta et al. 1991), the SOHO Extreme-ultraviolet Imaging Telescope (EIT; Delaboudiniere et al. 1995), and the *Transition Region and Coronal Explorer* (TRACE; Handy et al. 1999) have used an isothermal approximation. Results from SXT, a broadband X-ray imager, found that the temperature was highest at the loop top and decreased toward the footpoints (Kano & Tsuneta 1996). The temperature distributions derived from narrowband EUV imagers like EIT and TRACE, on the other hand, showed surprisingly little variation along their length (Neupert et al. 1998; Lenz et al. 1999). If the temperature profiles were this different, could the heating mechanisms also be different? In fact, could the fundamental physics that govern these loops be different as well?

Investigations began to answer these vital questions, but as the analysis methods became more sophisticated, the underlying physics took a back seat to the temperature studies. Zhang, White & Kundu (1999) developed a modified image-ratio technique that resulted in a two-component model for the plasma producing the coronal emission observed by EIT. Aschwanden & Nightingale (2005) applied a three-component model to TRACE loop data where the temperatures were fixed at the values corresponding to the peaks of the three response curves and the emission measure amplitudes were taken to be independent of each other. A later model by Aschwanden, Nightingale, & Boerner (2007) depended on a two-Gaussian temperature distribution for the loop strands.

The analysis methods described above, which found that a model with one, two, or three temperature components could explain the observations, were all limited by ad hoc assumptions. Schmelz, Kashyap & Weber (2007) constructed Differential Emission Measure (DEM) distributions for TRACE triple-filter loop data using a sophisticated Markov-Chain Monte Carlo (MCMC) based reconstruction algorithm (Kashyap & Drake 1998) available in SolarSoft. They found that these TRACE data could not, in general, limit the temperature distribution for coronal loop plasma. In other words, many different temperature distributions (isothermal, broad, sloped; etc.) could reproduce the observed fluxes, and the TRACE coronal data alone could not determine which of these distributions represented the actual coronal plasma. They found that it was not enough to show that a given model was consistent with the TRACE data; rather it must also eliminate the multi-thermal possibility. These authors caution against such simplistic analyses as they rely on ad hoc assumptions and tend to over-interpret the data.

In this paper, we use the xrt_dem_iterative2.pro (Weber et al. 2004) DEM routine available in SolarSoft as well as the MCMC DEM algorithm mentioned above to analyze

data from a coronal loop observed with the X-Ray Telescope (XRT; Golub et al. 2007) and the EUV Imaging Spectrometer (EIS; Culhane et al. 2007). These instruments were launched in September 2006 on the Japanese/USA/UK *Hinode* mission.

2. Observations

XRT is similar to SXT, but with greater sensitivity, nine different broadband filters, and a spatial resolution of two arc seconds. It was designed in part to constrain plasma temperatures more effectively than its predecessors. EIS has a similar spatial resolution and wavelength ranges of 170 - 210 and 250 - 290 Å. The EUV spectral lines observed by EIS are an excellent complement to the broadband X-ray data observed by XRT over a wide range of coronal temperatures. The combined data set provides both high- and low-temperature constraints, crucial for the multi-thermal analysis presented here.

The data used for this analysis were taken with XRT on 2007 May 13 at 16:16 UT of AR 10955 located at S09W30. The data set includes full Sun, full resolution images in all filters (except Al_Poly) as well as two filter combinations. The data processing included dark-frame subtraction, vignetting correction, and high-frequency noise removal using the standard xrt_prep.pro routine available SolarSoft. Spacecraft jitter was removed using xrt_jitter.pro, and long and short exposures (see Table 1) were co-aligned and combined to increase the image dynamic range. Additional Fourier filtering was done to the data from the thickest channel, Be_thick, to remove low-level, residual, longer-wavelength noise patterns. We have used the instrument calibration that modeled the time-dependent CCD contamination as a 1640-Å layer of diethylhexyl phthalate. (Note: A preliminary comparison with the recent update described in Narukage et al. (2010) indicates that this treatment is more than acceptable for the present work.) The response of XRT can be modeled using the make_xrt_wave_resp.pro and make_xrt_temp_resp.pro routines available in SolarSoft.

Figure 1 shows AR 10955 in the C_poly filter of XRT with the target loop outlined. Figure 2 shows the loop in several XRT filters, all taken 16:17-16:30 UT on 2007 May 13: (a) Al_mesh, (b) Ti_poly, (c) Be_thin, and (d) Al_thick. The loop is visible in all the XRT images except those taken through the thickest filter (Be_thick), which provides the high-temperature constraint for the DEM analysis (see below).

EIS also observed AR 10955 2007 May 13. At 14:25 UT the one arc sec slit began stepping across the active region, from right to left, building up the image. The entire process took approximately one hour to complete. The images are 250 × 250 square arcsec, with each spectral line observed in every pixel. The data were calibrated and the spectral

line intensities were determined with standard EIS software available in SolarSoft. The iron lines used in the analysis of this loop are listed in Table 2, and images of the region made in several of these lines are shown in Figure 3. The loop is visible in a number of these panels and appears to have a simple background structure.

Given the known response of XRT to optically thin thermal plasma (see Golub et al. 2007, Fig. 7), we can generate the possible DEM curves that can reproduce the observed fluxes in different XRT filters and filter combinations. For loops like the one analyzed here, XRT alone (with the two thickest channels, Al_thick and Be_thick filters) does an excellent job of constraining the high-temperature end of the DEM curve; the cool end, however, is not well-constrained. Adding in the EIS iron lines helps with this problem, giving us a good low-temperature constraint as well.

3. Analysis

We have used two different DEM routines: (1) xrt_dem_iterative2.pro (Weber et al. 2004) employs a forward-fitting approach where a DEM is guessed and folded through each response to generate predicted fluxes. This process is iterated to reduce the χ^2 between the predicted and observed fluxes. The DEM function is interpolated using several spline points, which are directly manipulated by the χ^2 fitting routine, mpfit.pro. There are N_i - 1 splines, representing the degrees of freedom for N_i observations. The routine uses Monte-Carlo iterations to estimate errors on the solution. A more detailed discussion and example use can be found in Schmelz et al. (2009b). (2) MCMC (Kashyap & Drake 1998) fits a locally smoothed DEM curve to the data by comparing the predicted to the observed fluxes and modifying the solution randomly to obtain new realizations. The smoothing scale varies with temperature to account for changes in the information content available as codified in the filter response curves. The new realizations are kept or discarded according to the Metropolis criterion based on changes in the χ^2 values at each step, resulting in a Markov-Chain that explores the parameter space efficiently. Typically we assumed 5% errors on the XRT data unless the photon noise was larger (true for Be_thick filter), and 10% errors on EIS lines. The larger errors were used to partly capture the effect of poorly known systematic errors (uncertainty in calibration, filter thickness, contamination layer thickness, etc.) Our analysis used the atomic data from version 5 of the Chianti data base (Dere et al. 1997; Landi et al. 2006), the ionization balance calculations of Mazzotta et al. (1998), and the "hybrid" abundances of Fludra & Schmelz (1999).

3.1. Global Loop Properties

Figure 2e shows the loop *spine* pixels, which were defined using a ridge fitting procedure. The user simply inputs the coordinates of the "start" and "stop" pixels and the code connects these with as short a line as possible; at each step, the code must chose the next pixel in the path to be the brightest out of all choices that get it closer to the target pixel. We experimented with various methods of background subtraction and settled on the following approach, which seemed most appropriate for the joint XRT-EIS data set. The data in each XRT/EIS channel in the selected field were normalized by their average value. With the data now all roughly on the same intensity scale, we averaged all the channels together into an overall mean image. The largest region of contiguous pixels near the loop and below 63% of the median level of the loop pixels became the initial background region. This region was then limited slightly in longitude and latitude, resulting in the background shown in Figure 2e (Note: the region extends slightly out of the frame to the north and west). For the final analysis here, we subtracted the average flux in the background region from the averaged loop spine flux for each of the different XRT filters/combinations and EIS iron lines.

Figure 4a shows the best fit (minimum χ^2) DEM curve generated by xrt_dem_iterative2.pro (color) and 300 Monte Carlo (MC) realizations (thin dash). Typically >95% of the realizations converged properly (i.e., yielding a "reasonable" $\chi^2 \leq \langle\chi^2\rangle + 2\sigma_{\chi^2}$). The range of MC realizations in each T bin gives one measure of the DEM uncertainty. Note that the MC simulations show low scatter about the best fit DEM for higher temperatures ($6.3 \leq$ Log T < 7.0), showing that XRT data alone does a good job of defining the higher-temperature loop plasma. At lower temperatures (Log T < 6.3), however, the results are quite different. The MC solutions diverge, spreading throughout the entire y-range of the plot. This indicates that XRT data alone do a relatively poor job of defining the cool loop plasma. This result is confirmed by a parallel analysis. We tested each temperature bin of the best fit DEM to see if it contributed significantly to one (or more) of the XRT filter fluxes. If a DEM temperature bin contributed at least 2% to the observed flux in any XRT filter, it is highlighted in orange. Note that the orange bins correlate well with those with low scatter in MC realizations. We also ran the MCMC code on the XRT data as a cross-check. These results (thick dash) show a slightly more "spiky" structure, but in general, there is good agreement with the xrt_dem_iterative2 DEM.

Figure 4b shows the best fit DEM curve (color) and the MC realizations (gray) generated by xrt_dem_iterative2.pro for the EIS iron line fluxes. Here the MC simulations have low scatter about the best fit DEM curve in the range $6.0 \leq$ Log T ≤ 6.5, but diverge at higher and lower temperatures. Here, a DEM temperature bin is highlighted in orange if it contributed at least 5% to any EIS line. As in Figure 4a, the bins which contribute

significantly to the observations are reasonably consistent with those with low scatter in their MC simulations (the high T "significant" bins contribute a small amount only to the hottest line). These preliminary results indicate that the combined XRT-EIS data set may effectively constrain the DEM fit at both high and low temperatures and provide a realistic model of the loop temperature distribution.

Figure 4c supports the effectiveness of such a combined XRT-EIS data set. It shows an EM Loci plot for the EIS iron lines (purples and blues) and the XRT filters (yellows, oranges, and reds). If the loop plasma were isothermal, than all the curves would intersect at a single point in the plot; this is clearly not the case. In addition, the loop emission measure distribution (with units of cm^{-5}) must fit under the curves. Looking at the EIS curves alone, one can see the effective EM "wall" the iron lines provide beginning at about Log T = 6.0, Log EM = 10^{26} cm^{-5} and building up to Log T = 6.5, Log EM = 10^{28} cm^{-5}. On the cool end, it is certainly possible for emission measure to "leak" under this wall, but the much bigger problem is that the high temperature half of the plot is completely unconstrained. Looking at the XRT curves alone shows the opposite problem: the XRT data provide little effective constraint on the cool half of the plot.

Figure 4d shows the fluxes predicted by the DEM model divided by the observed fluxes for the EIS lines (blue) and the XRT filters (orange) using the DEM curves in Figure 4a and 4b, respectively. The EIS points are in the order of peak formation temperature, from lowest to highest, and correspond to the entries in Table 2. The XRT points are ordered from the thinnest to thickest filters, corresponding to the order in Table 1. Overall, the EIS lines and XRT channels are ordered by increasing peak temperatures. The error bars reflect the observed uncertainties only. This result shows one of the many pitfalls in DEM analysis: it is possible to reproduce the observed fluxes quite well (no point is off by even as much as a factor of 2) and get a reasonable value of χ^2 even with a physically unrealistic, poorly constrained DEM model.

3.2. XRT-EIS Combined Data

Based on the results seen in Figure 4 and discussed above, we went on to combine the XRT and EIS data in order to generate a joint DEM model. Although these observations were not simultaneous, there were no GOES flares and the active region morphology appears stable. Figure 5 shows no evidence of significant loop evolution in the XRT Ti_poly images taken between the two data sets. Figure 6 shows the results for a cross-calibration factor of 1.0 on the left (implying that the relative calibration between the two instruments is perfect), and a cross-calibration factor of 1.6 on the right (see below). The top panels of

Figure 6 show the best fit DEM curves (color) and the MC realizations (gray) generated by xrt_dem_iterative2.pro. Here with the combined data set, the MC simulations follow the DEM curve quite well for Log T $>$ 6.0, but note the family of divergent solutions at very low temperatures. This results from the fact that our lowest temperature EIS line is Fe XI (see Table 2) with a peak formation temperature of Log T = 6.1, so the left-most portion of the plot is unconstrained. Cooler temperature EIS iron lines would solve this problem; Fe VIII would be an obvious choice, but Young et al. (2007) have raised concerns about the ionization balance calculations. We note that the forthcoming XRT calibration updates will affect (mainly) the thinnest filters and coolest temperatures. Since the EIS emissivities provide stronger DEM constraints at cool temperatures, we expect that the effect of these updates on the combined XRT-EIS data set will be small.

The middle panels of Figure 6 show the EM Loci as well as the emission measure distributions. As discussed above, the distribution must fit under the EM Loci curves (within uncertainties). These panels show how well the combined XRT-EIS data set constrains not only the plasma distribution for this particular loop, but they also show the promise for active regions in general which tend to have distributions that span the range 6.0 $\leq$ Log T $\leq$ 7.0. The yellow dashed curve represents the thickest XRT filter (Be_thick), which is essentially an upper limit; in this case, the errors fed to the MC simulations permit the emission measure distribution to breach the EM loci curve. The bottom panels show the model-to-observed flux ratios for EIS (blue) and XRT (orange), which result from the combined XRT-EIS DEM curves.

The XRT-EIS instrument cross-calibration factor was estimated using bright point data from Sun center taken on 2007 May 13. The advantages of using these data are that the bright point DEM has a simple shape and that no background subtraction is required (see, e.g., Saar et al. 2009). For XRT, we used the same full Sun images listed in Table 1. For EIS, we used the full spectrum data at 16:17 UT. The EIS lines from various ionization stages of iron, Fe X-Fe XIII, were used to construct an isothermal DEM curve for the peak of the observed bright point. Lines from Fe VIII and Fe XV were also available, but neither showed significant flux; these lines were used as the low-and high-temperature constraints, respectively. The resulting DEM was sharply peaked at Log T = 6.0 and used to predict the average bright point fluxes for the XRT filters. With the exception of the Al_mesh filter, for which contamination is a serious problem at these low temperatures, the XRT filter fluxes were, on average, a factor of 1.6 too low. Since the same abundance, ion fraction, and atomic data were used for both XRT and EIS, we conclude that this 1.6 offset is the XRT-EIS cross-calibration factor appropriate for these data.

The DEM realizations seen in Figure 6 are constrained by 9 XRT filters and filter

combinations and 8 EIS iron lines available for the loop spine. The resulting curves show that the loop DEM is neither sharply peaked nor extremely broad, with approximately 96% of the EM between $6.2 \leq \log T \leq 6.7$, and an EM weighted temperature of $\log T = 6.48 \pm 0.16$. There is no hint of the high-temperature DEM component, or nanoflare signature, found by Schmelz et al. (2009b) for the active region core. This result, or lack thereof, was expected since the loop is not clearly visible in the thickest XRT channel, Be_thick. These results could indicate that either the loop is cooling or that the nanoflare signature is too weak in the loop to be detected by XRT.

3.3. Loop Segments and Cuts

In this section, we compare the loop footpoint region with the loop top. To explore variations along the loop, we divided it into five roughly equal segments; these are depicted in Figure 2f. We averaged these sets of pixels and subtracted the average background. The resulting DEM shapes are similar to those of the global loop results seen in Figure 6, i.e., none could be considered isothermal. The DEM-weighted temperature, the "characteristic" temperature of the plasma along the line of sight, uses the following definition:

$$\langle logT_{DEM} \rangle = \sum_i \left(logT_i \times DEM(T_i) \right) / \sum_i \left(DEM(T_i) \right) \quad (1)$$

Figure 7 plots the DEM-weighted coronal temperature for the loop segments, from the left to the right footpoints. We find evidence for a small but systematic trend with temperature along the loop, with log T increasing only by ≈0.1 from the footpoints to the peak. Error bars in the figure reflect the scatter in $\langle T \rangle$ of the MC solutions; systematic errors due to uncertainties in the calibration, etc., may be larger (and incompletely known).

In the second step, we took several cuts across the loop at locations that had a relatively simple background structure. The profile was plotted (flux vs. position) for each filter and a straight line was fitted to the background. This background value was subtracted from the total flux at the peak position to produce the background-subtracted loop flux. Once again, DEM results are similar to those shown in Figure 6, where the loop DEM is neither isothermal nor extremely broad. DEM weighted average temperatures were seen to be generally higher near the top of the loop (consistent with Figure 7), though there was substantially more scatter due to the fewer number of pixels averaged into each analysis.

4. Discussion and Conclusions

XRT was designed in part to determine the DEM distributions of coronal plasma without the use of limiting ad hoc assumptions. The 2007 May 13 loop results in Figure 6 show a relatively broad, flat DEM structure, reminiscent of those obtained with spectral line data from the Coronal Diagnostics Spectrometer on SOHO (see, e.g., Fig. 2 of Schmelz & Martens 2006). This curve also resembles the DEM results obtained with the nanoflare simulations of Patsourakos & Klimchuk (2007; see, e.g., their Fig. 8), so there is theoretical support as well as observational evidence for these multithermal loop structures.

There are numerous coronal heating models, but observational constraints that can be applied to these models are rare. Following the reasoning described by Klimchuk (2006), if the coronal loops are overdense, the heating cannot be steady. For example, Winebarger et al. (2003a) looked at how X-ray loops observed with SXT and EUV loops seen with TRACE compared with static models. They found that only a small fraction (2 of 67) of their loops were consistent with static solutions with uniform heating and a filling factor of unity. Their longer, cooler (<3 MK) loops had densities that were up to 2500 times too high, and their shorter, hotter (>3 MK) loops had densities that were as much as 63 times too low. They also considered the possibility that the density disparities might be due to (steady) nonuniform heating along the loop, but found that footpoint heating could increase the densities by only a factor of 3, and loop-top heating could decrease the densities by only a factor of 2.5. Once again, only a small fraction (19 of 67) of the observed loops were consistent with hydrodynamic solutions with steady heating. They concluded that static loop models, including the classical Rosner, Tucker & Vaiana (1978) models, are poor representations of most active region loops. These results imply that the heating for these loops must be impulsive.

Even with the observational results described above, the "overdense" loops can still be modeled as a single flux tube, as long as the observed loop lifetimes are no longer than the predicted cooling times. Winebarger et al. (2003b) examined loops observed with TRACE that had flat 195/171 Å filter ratios and densities that were as much as 1000 times higher than those of static solutions to the hydrodynamic equations. These loops might have been impulsively heated flux tubes that were simply cooling through the TRACE passbands; this would imply that the loops must appear first in the hotter TRACE images before appearing in the cooler images. They tested and confirmed this idea by examining the temporal evolution of five active region loops observed in multiple TRACE EUV filter images. They then used the measured delay to estimate a cooling time and found that four of the five loops had observed lifetimes greater than the expected cooling times. These results have been confirmed with both imagers (Winebarger & Warren 2005) and spectrometers (e.g., Ugarte-

Urra et al. 2009), and imply that the loops cannot be composed of a single flux tube, even if the heating is dynamic. In this case, either the loops are multi-stranded, or we are missing some key component of the physics of coronal heating.

These multi-stranded loops, which appear to be necessary in the wake of the results described above, can be tested observationally. Multi-stranded loops should presumably be multi-thermal, at least some of the time (unless we are simply unlucky). Schmelz et al. (2001) used CDS and SXT data to construct DEM models at several positions along a coronal loop on the limb. Their temperature distributions were inconsistent with isothermal plasma along the line of sight and required a multi-stranded model. Subsequent analysis on background subtraction (Schmelz et al. 2005; Schmelz & Martens 2006), CDS data of other loops (Cirtain et al. 2007; Schmelz et al. 2007), and loop data from EIS (Schmelz et al. 2008; Rightmire & Schmelz 2010) confirm that the observations of at least some loops are not consistent with isothermal plasma, and therefore, cannot be modeled with a single flux tube. The DEM results from the combined XRT-EIS data set appear to agree with these multi-stranded loop models and multithermal loop observations. If it were not for observational results like those provided here, a crucial element of the coronal loop model described above would be lacking, and theorists might simply have to go back to the drawing board!

As we have seen during the course of this analysis as well as with observational loop results from other instruments, DEM is not a straightforward technique from which one can easily obtain dependable results. Our results show that the ultimate goal of DEM analysis cannot simply be a low value of χ^2. High- and low-temperature constraints are crucial to avoid non-physical (but still good χ^2) solutions at temperature extremes. Although we are in pursuit of the DEM as a function of temperature, it is also important to know the temperature regimes that produce little if any emission. In other words, we also need to know where the emission measure $isn't$. With the coronal loop analysis presented here, the thick XRT channels provided an excellent high-temperature constraint and there was no need to incorporate, e.g., RHESSI data as with the active region core results of Schmelz et al. (2009a). We did, however, require an additional low-temperature constraint for the loop DEM. This was provided by the EIS iron lines.

The other improvement inherent in our analysis is the lack of limiting ad hoc assumptions. We have not had to assume that the loop plasma is isothermal (e.g., Kano & Tsuneta 1996; Neupert et al. 1998; Lenz et al. 1999), or that we can model the DEM with a single Gaussian or a multi-component model (e.g., Aschwanden, Nightingale, & Boerner 2007; Aschwanden & Nightingale 2005). Unlike the DEM analysis of Schmelz, Kashyap & Weber (2007), who found that their TRACE triple-filter loop data could not limit the tempera-

ture distribution for coronal plasma, we find that the XRT-EIS data set does quite well. The combined data set does a much better job than either data set alone, and no ad hoc assumptions are required to produce the results presented here.

In conclusion, we find that the DEM of the loop spine is neither isothermal nor extremely broad, with approximately 96% of the EM between $6.2 \leq \log T \leq 6.7$. Adding the EIS data to our analysis is vital and helps better constrain the DEM at low temperatures. Finally, DEMs of the loop segments suggest there is a small increase in temperature of $\Delta \log T \approx 0.1$ from the loop footpoints to loop top. The next step in these investigations is to obtain data on a set of different loops from XRT and EIS to see if the variety of loop results from Skylab and subsequent instruments can be confirmed. AIA data now becoming available will also be powerful tool for these studies. The thicker XRT filters will be useful in constraining the hottest loop plasmas seen by AIA.

Hinode is a Japanese mission developed and launched by ISAS/JAXA, with NAOJ as domestic partner and NASA and STFC (UK) as international partners. It is operated by these agencies in co-operation with ESA and the NSC (Norway). CHIANTI is a collaborative project involving the NRL (USA), the Universities of Florence (Italy) and Cambridge (UK), and George Mason University (USA). Solar physics research at the University of Memphis is supported by a *Hinode* subcontract from NASA/SAO as well as NSF ATM-0402729. SS, MW, ED and LG are supported by contract NNM07AB07C to NASA. We benefited greatly from discussions at four workshops on solar coronal loops: Paris (November 2002), Palermo (September 2004), Santorini (June 2007), and Florence (June 2009).

REFERENCES

Aschwanden, M.J. & Nightingale, R.W. 2005, ApJ, 633, 499

Aschwanden, M.J., Nightingale, R.W. & Boerner, P. 2007, ApJ, 656, 577

Cirtain, J.W., Del Zanna, G., DeLuca, E.E., Mason, H.E., Martens, P.C.H., & Schmelz, J.T. 2007, ApJ, 655, 598

Culhane, J.L. et al. 2007, Sol. Phys., 243, 19

Dere, K.P., Landi, E., Mason, H.E., Monsignori Fossi, B.C., Young, P.R. 1997; A&A, 125, 149

Delaboudiniere, J.-P. et al. 1995, Solar Physics, 162, 291

Fludra, A. & Schmelz, J.T. 1999, A&A, 348, 286

Golub, L. et al. 2007, Sol. Phys., 243, 63

Handy, B.N. et al. 1999, Sol. Phys., 187, 229

Kano, R. & Tsuneta, S. 1996, PASJ, 48, 535

Kashyap, V. & Drake, J.J. 1998, ApJ, 503, 450

Klimchuk, J.A. 2006, Sol. Phys., 234, 41

Landi, E., Feldman, U., Dere, K.P. 2006; ApJS, 162, 261

Lenz, D.D., DeLuca, E.E., Golub, L., Rosner, R. & Bookbinder, J.A. 1999, ApJ, 517, L155

Mazzotta, P., Mazzitelli, G., Colafrancesco, S., Vittorio, N. 1998, A&A, 133, 403

Narukage, N. et al. 2010, in prep.

Neupert, W.M. et al. 1998, Solar Physics, 183, 305

Patsourakos, S. & Klimchuk, J.A. 2007, ApJ, 667, 591

Rightmire, L.A. & Schmelz, J.T. 2010, in prep.

Rosner, R., Tucker, W.H., & Vaiana, G.S. 1978, ApJ, 220, 643

Saar, S., Farid, S., Deluca, E. 2009, Proceedings of the 15th Cambridge Workshop on Cool Stars, Stellar Systems and the Sun. AIP Conference Proceedings, 1094, 756

Schmelz, J.T., Kashyap, V.L., Saar, S.H., Dennis, B.R., Grigis, P.C., Lin, L., De Luca, E.E., Holman, G.D., Golub, L., Weber, M.A. 2009a, ApJ, 704, 863

Schmelz, J.T., Kashyap, V. L. & Weber, M.A. 2007, ApJ, 660, L157

Schmelz, J.T. & Martens, P.C.H. 2006, ApJ, 636, L49

Schmelz, J.T., Nasraoui, K., Del Zanna, G., Cirtain, J.W., DeLuca, E.,E. & Mason, H. E. 2007, apj, 658, L119

Schmelz, J.T., Nasraoui, K., Richardson, V.L., Hubbard, P.J., Nevels, C.R. & Beene, J.E. 2005, ApJ, 627, L81

Schmelz, J.T., Saar, S.H., DeLuca, E.E., Golub, L., Kashyap, V.L., Weber, M.A., Klimchuk, J.A. 2009b, ApJ, 693, L131

Schmelz, J.T., Scopes, R.T., Cirtain, J.W., Winter, H.D. & Allen, J.D. 2001, 556, 896

Schmelz, J.T., Scott, J., Rightmire, L.A. 2008, ApJ, 684, L115

Smith, A.F.M. & Roberts, G.O. 1993, Journal of the Royal Statistical Society, Series B, 55, 3

Tsuneta, S. et al. 1991, 136, 37

Ugarte-Urra, I., Warren, H.P. & Brooks, D.H. 2009, ApJ, 695, 642

Weber, M. A., De Luca, E. E., Golub, L., & Sette, A. L. 2004, Multi-Wavelength Investigations of Solar Activity (Proc. IAU Symp. 223), ed. A. V. Stepanov, E. E. Benevolenskaya, & A. G. Kosovichev (Cambridge: Cambridge Univ. Press), 321

Winebarger, A.R. & Warren, H.P. 2005, ApJ, 626, 543

Winebarger, A.R., Warren, H.P. & Mariska, J.T. 2003a, ApJ, 587, 439

Winebarger, A.R., Warren, H.P. & Seaton, D.B. 2003b, ApJ, 593, 1164

Young, P.R., Del Zanna, G., Mason, H.E., Doschek, G.A., Culhane, L. & Hara, H. 2007, PASJ, 59, 727

Zhang, J., White, S.M. & Kundu, M.R. 1999, ApJ, 527, 977

Table 1. XRT Data from 2007 May 13

	Filter	Time (UT)	Exposure (long)	Time (UT)	Exposure (short)
8	Al_mesh	16:21:05	4.10 sec	16:20:11	0.18 sec
9	C_poly	16:26:20	8.20 sec	16:25:22	0.51 sec
10	Ti_poly	16:19:52	8.20 sec	16:19:42	0.51 sec
11	Al_poly-Ti	16:22:55	16.4 sec	16:21:50	1.45 sec
12	C-Ti	16:24:38	16.4 sec	16:23:37	1.03 sec
13	Be_thin	16:28:49	23.1 sec	16:28:13	1.03 sec
14	Be_med	16:30:23	46.3 sec	16:29:32	2.05 sec
15	Al_thick	16:18:44	46.3 sec	16:18:18	16.4 sec
16	Be_thick	16:17:02	65.5 sec	——	——

Table 2. EIS Data from 2007 May 13

	Ion	λ (Å)	Log T
0	Fe XI	180.40	6.1
1	Fe XII	195.12	6.1
2	Fe XIII	202.04	6.2
3	Fe XIII	203.83	6.2
4	Fe XIV	264.78	6.3
5	Fe XIV	274.20	6.3
6	Fe XV	284.16	6.3
7	Fe XVI	262.98	6.4

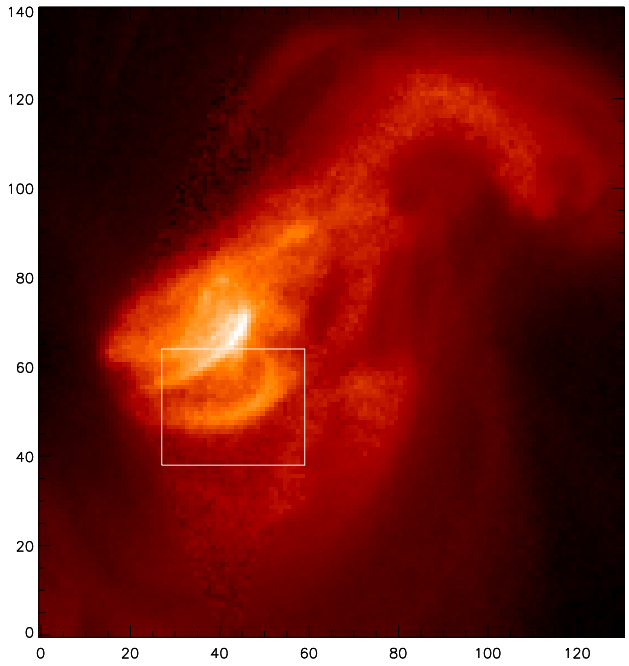

Fig. 1.— XRT observation of AR 10955 located at S09W30 on 2007 May 13. The target loop is outlined in the image taken with the C_poly filter at 16:25 UT. The intensity is scaled logarithmically to improve weak feature visibility. The image is a composite of long and short exposures to enhance the dynamic range.

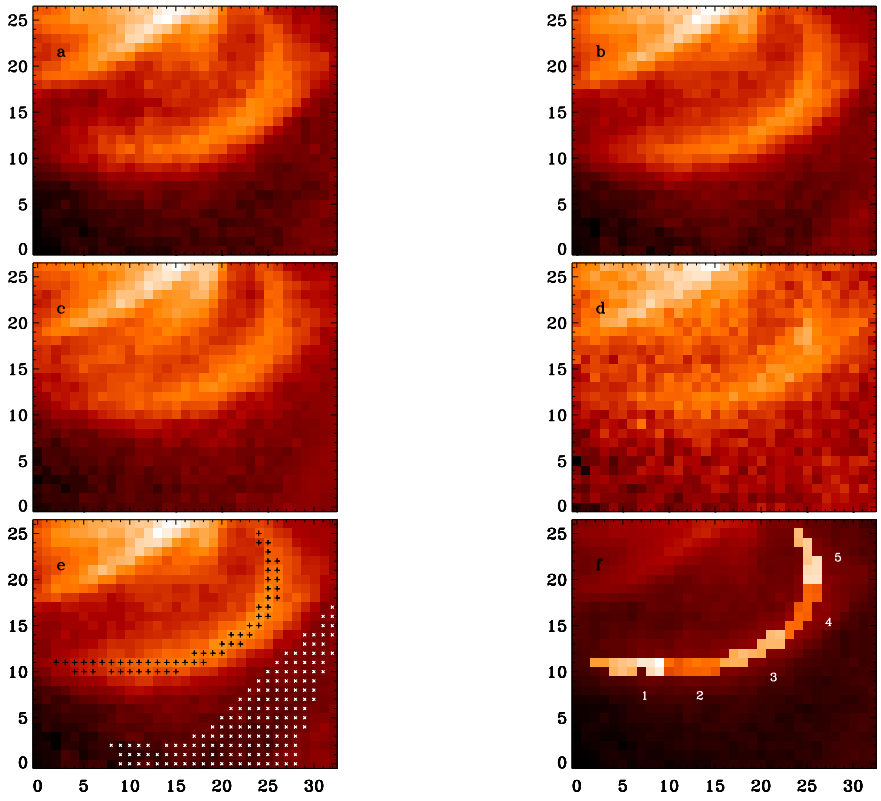

Fig. 2.— The loop in several XRT filters (log scaled): (a) Al_mesh, (b) Ti_poly, (c) Be_thin, and (d) Al_thick; (e) the loop spine and background (see text); (f) the loop segments. Image times are listed in Table 1.

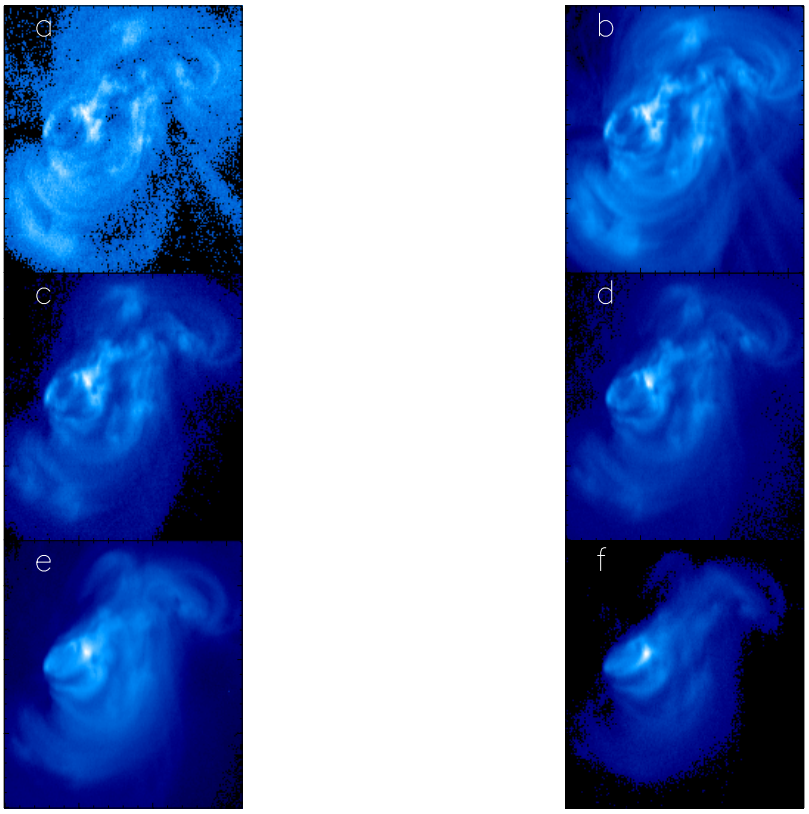

Fig. 3.— EIS data of AR 10955 taken with the one arc sec slit on 2007 May 13, starting at 14:25 UT. The images are 250 × 250 square arcsec. The intensity is scaled logarithmically to improve weak feature visibility. Panels show the images in EIS iron lines used in the analysis of this loop, from coolest to hottest. (a) Fe XI, (b) Fe XII, (c) Fe XIII, (d) Fe XIV, (e) Fe XV, and (f) Fe XVI. The loop is most easily seen in panel (e), just below the bright peak.

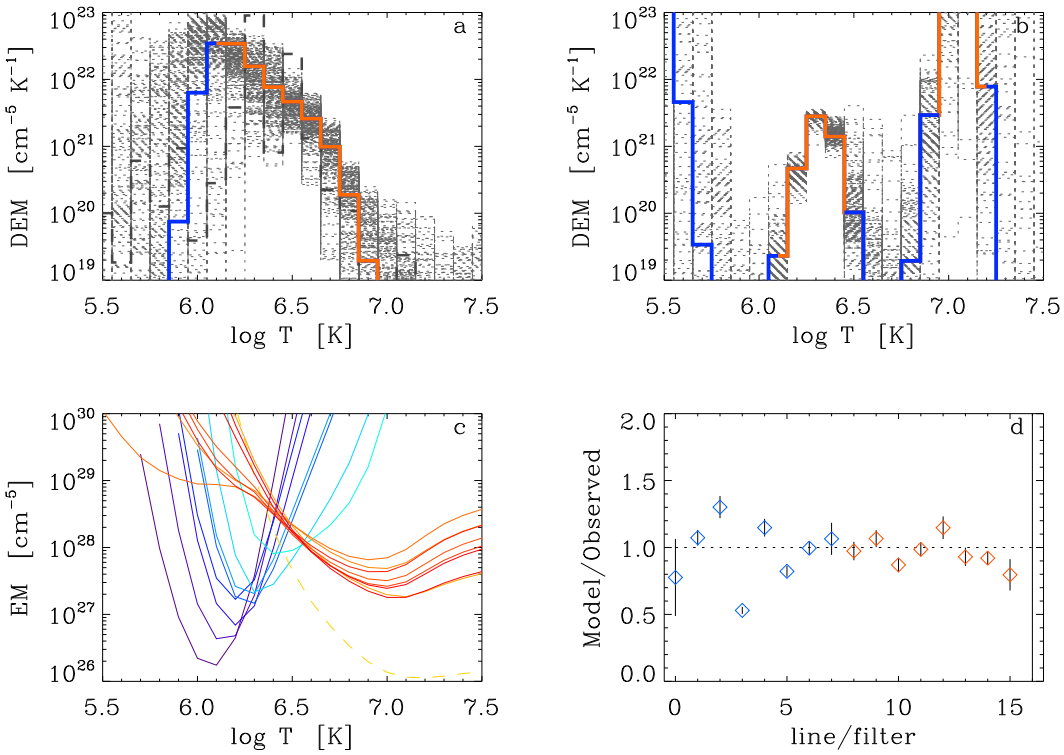

Fig. 4.— (a) Best fit DEM curve generated by xrt_dem_iterative2.pro (color) and MCMC (thick dash) for XRT alone. The thin dash results are the MC realizations from xrt_dem_iterative2.pro, which give a measure of the DEM uncertainty. The orange portions of the DEM curve depict temperature bins which contribute at least 2% of the flux to any XRT filter (the blue portions contribute <2%); (b) Best fit DEM curve (color) and the MC realizations (gray dashed) generated by xrt_dem_iterative2.pro for EIS alone. The orange portions of the DEM curve depict temperature bins which contribute at least 5% of the flux to any EIS line (the blue portions contribute <5%). (c) EM Loci for the EIS iron lines (purples and blues) and the XRT filters (yellows, oranges, and reds). The yellow dashed curve depicts the upper limit for the thickest XRT filter, Be_thick; (d) Model-to-observed flux ratio for EIS lines (blue) and XRT filters (orange) using the DEM curves in (a) and (b), respectively. Numbering corresponds to the order in Tables 1 and 2. The line at position number 16 whose error spans the entire plot represents the upper limit for the thickest XRT filter, Be_thick.

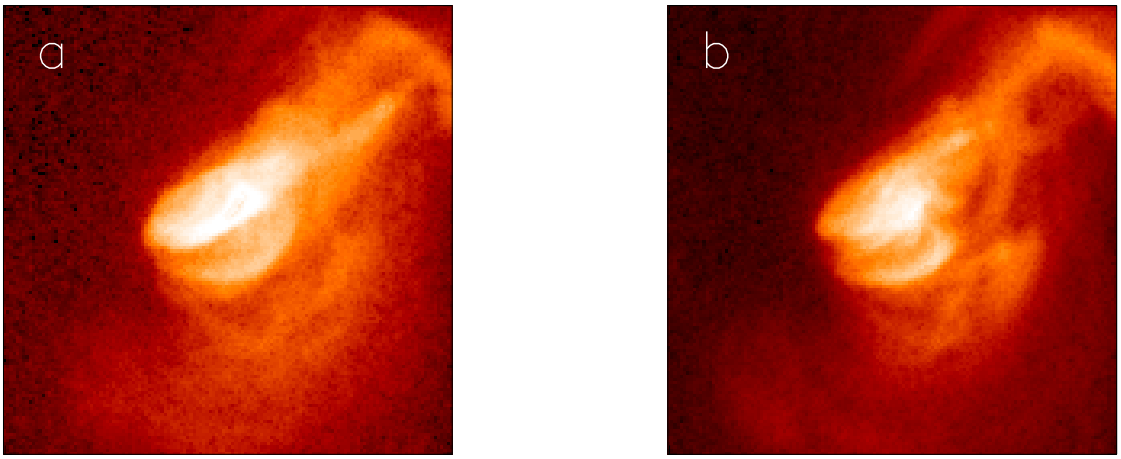

Fig. 5.— XRT images in Ti_poly taken on 2007 May 13 at (a) 14:25:53 and (b) 16:14:06, the times of the EIS raster and XRT image sequence, respectively. Both images are the same size and same resolution. The first, however, had a longer exposure time so both images were normalized with units of DN/sec. The images show that the loop remained stable during the observations used in the analysis.

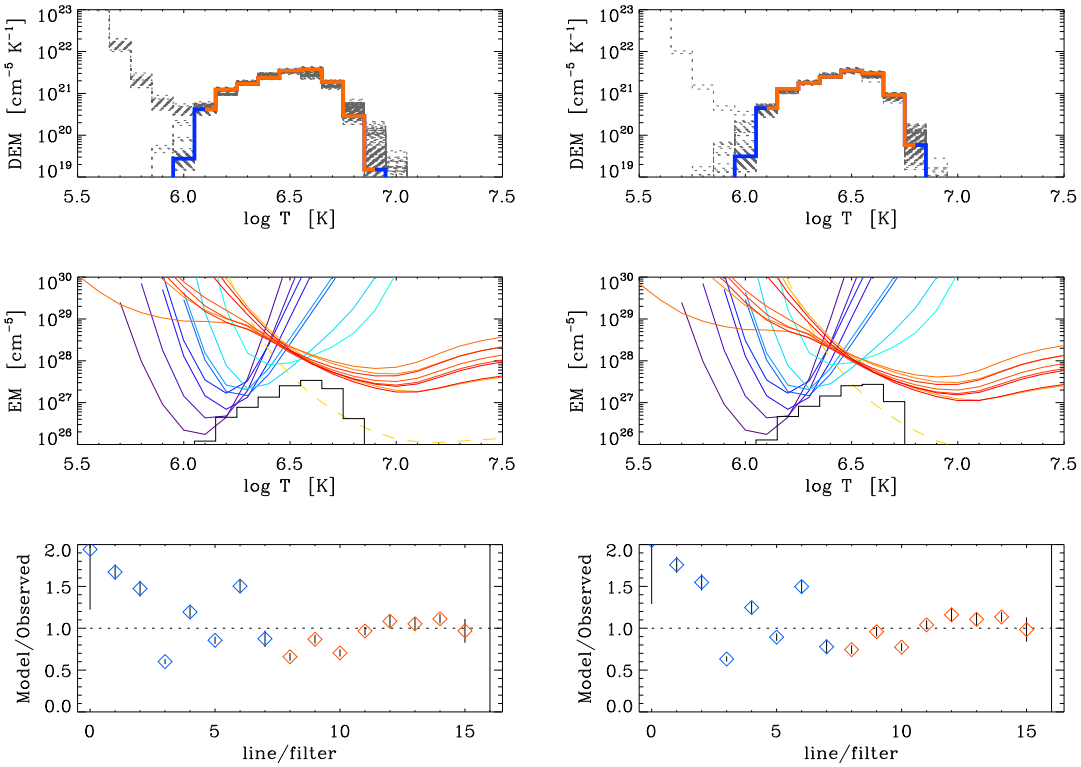

Fig. 6.— Combined XRT-EIS results for a cross-calibration factor of 1.0 (left) and 1.6 (right). Top: best fit DEM curves (color) and the MC realizations (gray dashed) generated by xrt_dem_iterative2.pro. The color coding is the same as that in Figure 4. Middle: EM Loci and emission measure distributions. As in Figure 4, the yellow dashed curve depicts the upper limit for Be_thick; Bottom: model-to-observed flux ratios for EIS (blue) and XRT (orange), which result from the combined XRT-EIS DEM curves. The line at position number 16 represents Be_thick.

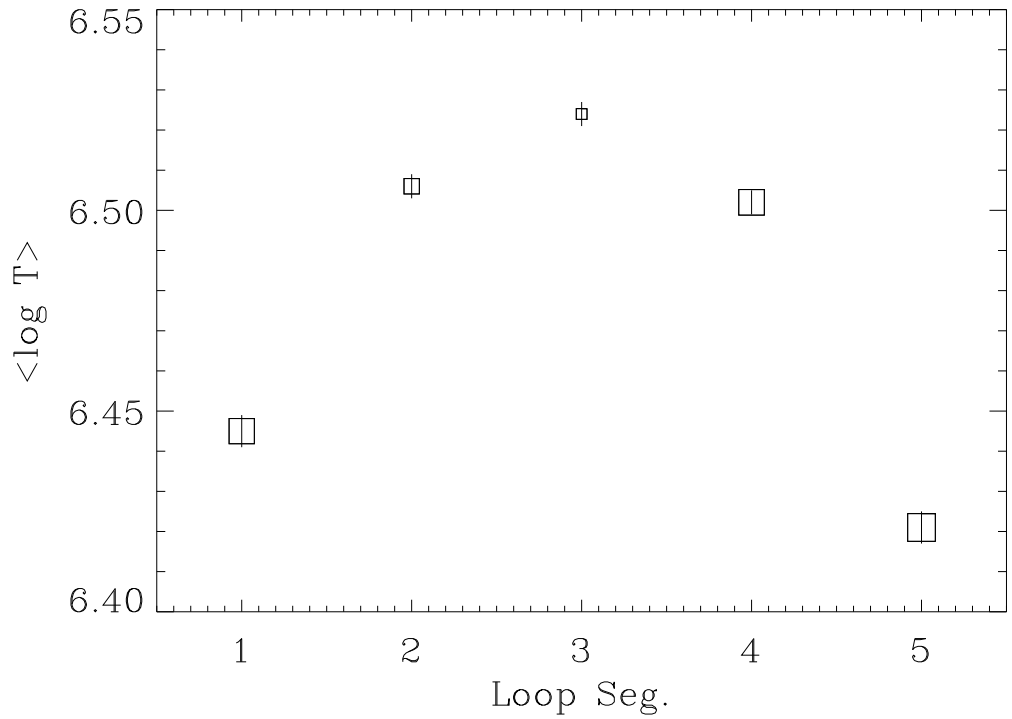

Fig. 7.— DEM-weighted coronal temperature for the loop segments shown in Figure 2f, from the left to right footpoints. There is a small but systematic trend with temperature along the loop. The error bars reflect the spread standard deviation of the $\langle T \rangle$ among the MC realizations, and thus do not include systematic errors.